

**Sea ice microstructure: resolving anisotropic structure through cross-borehole dc
resistivity tomography**

K.A. Jones¹, M. Ingham¹ and D.J. Pringle²

¹School of Chemical & Physical Sciences, Victoria University of Wellington, PO Box 600,
Wellington, New Zealand

²Geophysical Institute and Arctic Region Supercomputing Centre, University of Alaska,
Fairbanks, Alaska, USA

Abstract

The distribution and connectivity of brine pockets in first-year sea ice has a determining influence on the bulk properties of the ice and its interaction with the environment. The structure of the brine network depends upon both temperature and salinity, and a full understanding of the temporal evolution of sea ice physical properties requires measurements that are sensitive to the microstructure, and can also be made without disturbing the natural state of the ice. Direct current resistivity techniques are suited to this as the brine fraction is orders of magnitude more conductive than solid ice. However, due to the preferential vertical alignment of brine inclusions, the bulk resistivity of first-year sea ice is anisotropic. Although this makes the interpretation of surface resistivity soundings extremely difficult, consideration of the theory of resistivity measurements in an anisotropic medium shows that the anisotropic resistivity structure may be resolved through cross-borehole measurements. Borehole pairs with one current and one potential electrode in each hole allow the determination of the horizontal component of the anisotropic bulk resistivity (ρ_H). Four boreholes located on the corners of a square are shown to provide a method by which estimates of the geometric mean of the bulk resistivity (ρ_m) may also be derived. Combining derived variations with depth of ρ_H and ρ_m allows calculation of the vertical resistivity (ρ_V), giving a complete picture of the resistivity structure of the ice. This is illustrated by results cross-borehole measurements made in first-year sea ice near Barrow, Alaska in May 2008.

1. Introduction

Sea ice covers a large area of high latitude ocean in the Arctic and Antarctic regions and acts as an interface between the ocean and the atmosphere, regulating the exchange of heat, moisture and salt. While sea ice extent varies seasonally, at maximum approximately 7% of the Earth's surface is covered. Sea ice is thus one of the largest biomes on Earth and due to its influence on the interaction between ocean and atmosphere it is an important component in research of past, present and future climate (Dieckmann and Hellmer, 2003).

During the formation of sea ice, brine becomes trapped in pockets within the solid ice matrix. These range in size from sub-millimeter pores to large connected networks of channels several millimeters in diameter and extending over several decimeters. The connectivity of the brine pockets is highly sensitive to variations in temperature and bulk ice salinity, and strongly affects physical, optical, (Eicken, 2003) and biological properties (Krembs et al., 2000) of sea ice. It is through these properties that sea ice has a determining influence on the global climate (Comiso, 2003) and ecosystems. An understanding of the manner in which the internal microstructure of sea ice changes in response to changes in temperature and salinity is therefore crucial for a fuller understanding of the role that sea ice plays in a range of contexts. The existence and connectivity of brine channels in the ice affects the transport of heat through the ice (Perovich, 1998; Weeks, 1998). By estimating the latent heat release associated with convective overturning and refreezing of brine, Pringle et al. (2007) have estimated that internal brine motion within the ice may somewhat enhance the overall heat flux. Brine inclusions also control the manner in which the ice interacts with electromagnetic radiation (Hallikainen & Winebrenner, 1992; Cherkaeva &

Golden, 1998), while the fluid permeability is important for nutrient transport through the ice (Fritsen et al., 1994). Theoretical calculations of the physical properties of sea ice have generally been based on effective medium theories (e.g. Tinga et al., 1973) and, more recently, on percolation theory (Golden et al., 1998, 2007). Nevertheless there are few field measurements of the temporal variation in the physical properties of sea ice with which such theoretical calculations can be compared.

The internal structure of sea ice ought to be able to be studied using any transport property to which the brine and ice components contribute differently. The microstructure, thermal evolution, fluid transport and permeability of sea ice brine inclusions have been studied by several authors using NMR techniques (Callaghan et al., 1998, 1999; Eicken et al., 2000; Mercier et al., 2005), bail-test and fluorescent tracer methods (Freitag and Eicken, 2003), x-ray computed tomography (Kawamura, 1988, Pringle et al., submitted), and measurement of the complex dielectric permittivity (Pringle et al., 2009). However, in practice there are severe difficulties in making accurate measurements as most such methods inevitably disturb the ice in its natural state, such as brine loss from samples that need to be extracted for measurements in the laboratory or artificial brine motion induced by insertion of large probes.

In this context, measurements of electrical resistivity hold some promise, since the large resistivity contrast between brine and solid ice opens a path towards indirect probing of other key ice properties. Furthermore, direct current (dc) geoelectric soundings, widely used in shallow geophysical studies, are generally made using surface electrodes and do not therefore disturb the natural structure of the sub-surface. However, due to the preferential vertical alignment of brine

inclusions, the bulk resistivity of sea ice is anisotropic and, as a result, surface resistivity soundings can be shown (e.g. Bhattacharya and Patra, 1968) to be sensitive to only the geometric mean resistivity of the anisotropic medium. This has been clearly noted in previous resistivity measurements made on sea ice (e.g. Fujino and Suzuki, 1963; Thyssen et al., 1974; Timco, 1979; Buckley et al., 1986, Ingham et al., 2008) which have also shown that surface soundings underestimate the true thickness of the anisotropic sea ice cover. This makes the interpretation of soundings in terms of variation of geometric mean resistivity with depth problematic.

Recently Ingham et al. (2008) have demonstrated that an alternative dc resistivity technique, that of cross-borehole tomography, can be used to measure the horizontal component of the anisotropic resistivity structure of sea ice. This technique involves making resistivity measurements using vertical strings of electrodes frozen into the ice while it is relatively thin and that are subsequently embedded into the growing ice sheet. Although insertion of electrode strings, and their subsequent freezing in, disturbs the ice structure immediately adjacent to the boreholes, the bulk of ice between the electrode strings is undisturbed and it is through this that current passes. Such measurements therefore largely sample ice in its natural state. Ingham et al. (2008) reported trial measurements made at Barrow, Alaska that clearly suggested that changes in the horizontal component of resistivity of the ice occurred over the period of spring warming.

In this paper we discuss the further development of resistivity techniques to study the physical properties of sea ice. We start by readdressing, from the point of view of the theory of resistivity measurements in an anisotropic medium, the ability or inability of cross-borehole techniques to measure not only the horizontal component of the anisotropic resistivity, but also the vertical

component and the geometric mean resistivity. Following consideration of an infinite anisotropic medium we consider an anisotropic medium bounded by air above and by a highly conducting half-space, representative of sea water, below. We demonstrate how in this situation, in addition to resolving the horizontal component of resistivity, cross-borehole measurements supported by the results of model calculations can yield the geometric mean resistivity and its variation with depth in the ice. This consequently allows the derivation of the vertical component of the resistivity, thus determining the complete resistivity structure. We illustrate this both with inversions of synthetic data generated from forward numerical calculations, and an example of the actual application to real sea ice. The results indicate that the resistivity technique holds much promise for investigating and understanding the temporal variation of the microstructure of sea ice.

2. Electrical resistivity measurements in an infinite uniform anisotropic medium

In first-year sea ice, formed under quiescent conditions the preferential vertical alignment of the brine inclusions means that the bulk resistivity structure of the ice is anisotropic, with the vertical component of the bulk resistivity lower than the horizontal component. Although it is possible that in the presence of steady ocean currents the horizontal resistivity itself may exhibit some anisotropy, particularly in the case of landfast sea ice, in the present analysis we treat this as typically insignificant compared to the anisotropy between the vertical and horizontal resistivity.

Following Bhattacharya & Patra (1968), in an infinite uniform anisotropic medium in which the principal resistivities (ρ_H , ρ_V) are horizontal and vertical the potential at a location (x_j , y_j , z_j) due to a current I injected into the medium from a single electrode at (x_i , y_i , z_i), is given by

$$V = \frac{I\rho_m}{4\pi r_{ij} \left\{ 1 + (\lambda^2 - 1) \frac{(z_i - z_j)^2}{r_{ij}^2} \right\}^{1/2}} \quad (1)$$

where ρ_m is the geometric mean resistivity

$$\rho_m = \sqrt{\rho_H \rho_V} \quad (2)$$

λ is an anisotropy coefficient defined as

$$\lambda = \sqrt{\frac{\rho_V}{\rho_H}} \quad (3)$$

and

$$r_{ij} = \sqrt{(x_i - x_j)^2 + (y_i - y_j)^2 + (z_i - z_j)^2}.$$

Equation (1) may be expressed in the simpler form

$$V = \frac{I\rho_m}{4\pi \{X_{ij}^2 + \lambda^2(z_i - z_j)^2\}^{1/2}} \quad (4)$$

where

$$X_{ij} = \sqrt{(x_i - x_j)^2 + (y_i - y_j)^2} \quad (5)$$

is the horizontal separation between the current and potential electrodes.

The majority of electrical imaging surveys make use of four electrodes. Two electrodes are used to introduce current into the medium, one being a current source the other a sink. The potential difference is then measured between the remaining two electrodes. For a four electrode system in

which current is injected into an anisotropic medium through an electrode C_1 at (x_1, y_1, z_1) , is taken out of the medium through an electrode C_2 at (x_2, y_2, z_2) , and in which the potential difference ΔV is measured between electrodes P_1 and P_2 at (x_3, y_3, z_3) and (x_4, y_4, z_4) respectively, equation (1) may be used to show that

$$\Delta V = \frac{I}{4\pi} \rho_m (T_{13} - T_{14} - T_{23} + T_{24}) \quad (6)$$

where

$$T_{ij} = \frac{1}{r_{ij} \left\{ 1 + (\lambda^2 - 1) \frac{(z_i - z_j)^2}{r_{ij}^2} \right\}^{1/2}}$$

Starting from (6) it is possible to investigate which, if any, combinations of electrodes embedded in an infinite uniform anisotropic medium will allow the direct measurement of individual components of the anisotropic resistivity. This is done by considering the fact that if measurements were made in a medium of uniform isotropic resistivity ρ then the equivalent form of equation (6) would be

$$\Delta V = \frac{I}{4\pi} \rho \left\{ \frac{1}{r_{13}} - \frac{1}{r_{14}} - \frac{1}{r_{23}} + \frac{1}{r_{24}} \right\} \quad (7)$$

Determining the conditions under which (6) reduces to (7) when ρ is considered to be ρ_m , ρ_V or ρ_H , shows which electrode combinations, if any, it is possible to use to yield a determination of the relevant resistivity.

Although our interest is primarily in the microstructure of sea ice, for which $\lambda < 1$, in the development that follows we also note the implications for anisotropic resistivity structures for which the vertical resistivity is greater than the horizontal resistivity ($\lambda > 1$).

2.1. Measurement of ρ_H

The measurement of the horizontal component of the anisotropic resistivity has previously been discussed by Ingham et al. (2008). We summarise those arguments here. As outlined above measurements can be interpreted in terms of the horizontal component if equation (6), rewritten using (2) and (3) as

$$\Delta V = \frac{I}{4\pi} \rho_H \lambda (T_{13} - T_{14} - T_{23} + T_{24}) \quad (8)$$

is identical to the following form of equation (7)

$$\Delta V = \frac{I}{4\pi} \rho_H \left\{ \frac{1}{r_{13}} - \frac{1}{r_{14}} - \frac{1}{r_{23}} + \frac{1}{r_{24}} \right\} \quad (9)$$

This will be true if in each of the T_{ij} terms in (8)

$$1 + (\lambda^2 - 1) \frac{(z_i - z_j)^2}{r_{ij}^2} = \lambda^2 \quad (10)$$

This is satisfied if

$$(z_i - z_j)^2 = r_{ij}^2$$

which implies that either

$$(x_i - x_j)^2 + (y_i - y_j)^2 = 0 \quad (11a)$$

or, alternatively, that

$$|z_i - z_j| \gg \sqrt{(x_i - x_j)^2 + (y_i - y_j)^2} \quad (11b)$$

Condition (11b) is met when the current and potential electrodes are much more widely separated vertically than they are horizontally. Although the present discussion concerns an anisotropic medium of infinite extent it is clear that this condition will have practical limitations in a real situation in which the anisotropic structure under study is relatively thin. As this is the case for first-year sea ice, for which typical thicknesses are < 2 m, we do not consider this possibility.

Condition (11a) corresponds to the current electrode and the potential electrode having the same horizontal location i.e. being in the same borehole. Applying the same condition to all four T_{ij} terms in equation (8) requires all four electrodes to be in a single borehole. Timco (1979) effectively met this condition by using four electrodes aligned vertically in the side of an ice pit to measure ρ_H . However, in the case of four electrodes within the same borehole the formation of an anomalous halo around the electrode string when it is frozen into the ice raises the likelihood that measurements will be significantly affected by ice that is not in its natural state. We therefore exclude this option also.

An additional possibility, as described by Ingham et al. (2008), is to consider the situation where C_1 and P_1 have the same horizontal location (i.e. $x_1 = x_3$, $y_1 = y_3$), as do C_2 and P_2 ($x_2 = x_4$, $y_2 =$

y_4). In a practical situation this is equivalent to using 2 boreholes, each containing one current and one potential electrode. This simplifies the expressions for T_{13} , and T_{24} to

$$\lambda T_{ij} = \frac{1}{|z_i - z_j|}$$

while those for T_{14} and T_{23} become

$$\lambda T_{ij} = \frac{\lambda}{\left\{ (X_1 - X_2)^2 + (z_i - z_j)^2 \right\}^{1/2} \left\{ 1 + (\lambda^2 - 1) \frac{(z_i - z_j)^2}{(X_1 - X_2)^2 + (z_i - z_j)^2} \right\}^{1/2}}$$

where $X_1 - X_2$ is the horizontal distance between the boreholes.

The expressions for λT_{13} and λT_{24} are clearly equal to the first and last terms on the right hand side of (9). Ingham et al. (2008) demonstrate that, given $\lambda < 1$ and a separation of the boreholes that is 10 times the smallest vertical electrode separation i.e.

$$\frac{|z_i - z_j|}{|X_1 - X_2|} = n0.1 \quad (12)$$

where n is an integer, the dependency on λ in the expressions for λT_{14} and λT_{23} may be approximated as

$$\frac{\lambda}{\left\{ 1 + (\lambda^2 - 1) \frac{(z_i - z_j)^2}{(X_1 - X_2)^2 + (z_i - z_j)^2} \right\}^{1/2}} \approx \frac{\lambda}{\left\{ 1 + (\lambda^2 - 1) \frac{0.01n^2}{1 + 0.01n^2} \right\}^{1/2}} \sim \lambda$$

Normalising, using $|X_1 - X_2| = 1$, the ratios of the terms in T_{14} and T_{23} to those in T_{13} and T_{24} are

$$(\lambda T_{14}, \lambda T_{23}) : (\lambda T_{13}, \lambda T_{24}) \sim \frac{n\lambda}{10} \quad (13)$$

218 If current and potential electrode pairs are chosen such that $n \leq 2$ then, for reasonable values of
 219 anisotropy, with $\rho_V < \rho_H$, terms in T_{14} and T_{23} may be ignored compared to those in T_{13} and T_{24} .

220

221 It also follows that for $|X_1 - X_2| = 1$, and values of $n \leq 2$ the terms in (9) in $\frac{1}{r_{14}}$ and $\frac{1}{r_{23}}$ will be

222 significantly less than 1/5 of the size of the terms in $\frac{1}{r_{13}}$ and $\frac{1}{r_{24}}$. Ignoring these smaller terms in

223 equation (9) gives an error of $\sim 10\%$ in the spatial term and within this error equations (8) and (9)

224 may both be approximated by

$$225 \quad \Delta V = \frac{I}{4\pi} \rho_H \left\{ \frac{1}{|z_1 - z_3|} + \frac{1}{|z_2 - z_4|} \right\} \quad (14)$$

226 Thus the use of electrodes at two horizontal locations under the conditions that (i) $\lambda < 1$; and (ii)
 227 the electrodes are positioned such that equation (12) holds, with n small; allows measurements to
 228 be made which are sensitive to ρ_H .

229

230 In the situation where $\lambda > 1$ (i.e. the vertical resistivity is greater than the horizontal) there is no
 231 simple relationship giving the ratio of the terms in T_{14} and T_{23} to those in T_{13} and T_{24} . Calculation
 232 shows that for all values of n in (13) the ratio is significantly larger than for the case $\lambda < 1$. It is
 233 clear from this that when $\lambda > 1$ there are in fact no combinations of electrodes which allow the
 234 terms in T_{14} and T_{23} to be reasonably ignored compared to those in T_{13} and T_{24} . Thus there are no
 235 electrode combinations that allow a good estimate of ρ_H to be obtained when the horizontal
 236 resistivity is less than the vertical resistivity.

237

2.2. Measurement of ρ_m

To provide a measure of the geometric mean resistivity ρ_m , equation (6) must be equivalent to the expression

$$\Delta V = \frac{I}{4\pi} \rho_m \left\{ \frac{1}{r_{13}} - \frac{1}{r_{14}} - \frac{1}{r_{23}} + \frac{1}{r_{24}} \right\}$$

This requires conditions on the denominators of the expressions for the T_{ij} of the form

$$1 + (\lambda^2 - 1) \frac{(z_i - z_j)^2}{r_{ij}^2} = 1 \quad (15)$$

Equation (15) may be satisfied if

$$z_i = z_j$$

Extending this so that the conditions are imposed upon all four T_{ij} terms implies that all four electrodes must be at the same vertical level

$$z_1 = z_2 = z_3 = z_4$$

As it is undesirable to use the same electrode for both current injection and potential measurement, in order to make measurements that will determine ρ_m it is therefore necessary to use a minimum of 4 electrodes at separate horizontal locations (i.e. a minimum of 4 boreholes). In the most general situation where ρ_m is $\rho_m(x, y, z)$, for n boreholes, discounting measurements which simply reverse either the current or potential electrodes, there are therefore $n!/4$ independent measurements that may be made for each vertical level at which there is an electrode.

Measurements of ρ_m may also be obtained by removing either or both of one current and one potential electrode to infinity. For example, under the circumstance of C_2 being at infinity, the expressions for both T_{23} and T_{24} are zero and as long as $z_1 = z_3 = z_4$ then T_{13} and T_{14} are $1/r_{13}$ and $1/r_{14}$ respectively, and both equations (6) and (7) reduce to

$$\Delta V = \frac{I}{4\pi} \rho_m \left\{ \frac{1}{r_{13}} - \frac{1}{r_{14}} \right\}$$

Similarly, if P_2 is at infinity and $z_1 = z_2 = z_3$ (6) and (7) reduce to

$$\Delta V = \frac{I}{4\pi} \rho_m \left\{ \frac{1}{r_{13}} - \frac{1}{r_{23}} \right\}$$

Clearly therefore, using 4 or more electrodes all at separate horizontal locations, there are electrode combinations that may be used to measure the geometric mean resistivity of an infinite uniform anisotropic medium. This result does not depend upon the magnitude of the anisotropy coefficient and applies equally to anisotropic resistivity structures for which $\lambda < 1$ or $\lambda > 1$.

2.3. Measurement of ρ_V

To ascertain which, if any, electrode combinations may be used to make measurements which can be used to derive the vertical component of the resistivity ρ_V it is necessary to use equations (2) and (3) to recast equation (6) in the form

$$\Delta V = \frac{I}{4\pi} \frac{\rho_V}{\lambda} (T_{13} - T_{14} - T_{23} + T_{24})$$

279 For this equation to take the form which would indicate that measurements are responsive to ρ_V ,
 280 namely

$$281 \quad \Delta V = \frac{I}{4\pi} \rho_V \left\{ \frac{1}{r_{13}} - \frac{1}{r_{14}} - \frac{1}{r_{23}} + \frac{1}{r_{24}} \right\}$$

282 requires that expressions of the form

$$283 \quad \frac{1}{1 + (\lambda^2 - 1) \frac{(z_i - z_j)^2}{r_{ij}^2}} = \lambda^2 \quad (16)$$

284 are satisfied. Equation (16) reduces to

$$285 \quad \frac{(z_i - z_j)^2}{r_{ij}^2} = -\frac{1}{\lambda^2} \quad (17)$$

286 which clearly does not have a real solution. It may therefore be concluded that there are no
 287 possible electrode combinations that may be interpreted in terms of the vertical component of the
 288 anisotropic resistivity. Again, this is true whatever the value of λ .

289

290 **3. Cross-borehole measurements in a bounded anisotropic medium**

291

292 In reality cross-borehole resistivity tomography seeks to image the relatively near-surface
 293 structure in a half-space of variable resistivity. Although the above theory suggests that
 294 measurement of the horizontal component and geometric mean resistivity are possible in an
 295 infinite anisotropic medium, this will not necessarily be the case in a bounded anisotropic
 296 medium. It is necessary therefore to see how the above results are modified by the inclusion of
 297 boundaries.

298

To consider the effect of boundaries on the potential at a given point in the medium due to a current source elsewhere in the medium we make use of an analogy made in many applied geophysics texts (e.g. Telford et al., 1977) between current flow through a boundary between two media and the optical case of a point light source in one medium separated from another medium by a semi-transparent mirror with reflection coefficient k_1 . In the optical case the light intensity at a point in the first medium is a combination of the intensity due to the point source and the intensity due to its image in the mirror, diminished by the reflection coefficient. Similarly, the electric potential at a point in the same medium as a point current source can be considered as the sum of the potential due to the source and a generally diminished potential due to an image source. The intensity or potential at a point in the second medium is due only to the point source, but diminished by the transmission coefficient of the boundary.

This situation is illustrated in Fig. 1 in which two semi-infinite media are separated by a boundary at $z = 0$ with a reflection coefficient k_1 . Current is injected and potential measured in the lower medium which is assumed to be anisotropic. The potential at electrode P at (x_j, z_j) due to current I injected at electrode C at (x_i, z_i) may be expressed, using the form of equations (4) and (5), as

$$V = \frac{I\rho_m}{4\pi\{X_{ij}^2 + \lambda^2(z_i - z_j)^2\}^{1/2}} + \frac{k_1 I\rho_m}{4\pi\{X_{ij}^2 + \lambda^2(z_i + z_j)^2\}^{1/2}} \quad (18)$$

In (18) the first term is the potential due to the actual electrode through which current is injected. The second term is the potential due to the image of C in the boundary. k_1 is the reflection coefficient in the boundary. For the practical case of the upper medium being air, $k_1 = 1$.

321

322 The addition of a second boundary at depth t with reflection coefficient k_2 modifies (18) further.323 In this situation the anisotropic medium is confined to the region $0 \leq z \leq t$ and multiple images

324 of the current source occur in both boundaries. As given for example by Keller & Frischknecht

325 (1966), the potential observed at an electrode (P) in the anisotropic medium at (x_j, y_j, z_j) due to326 current injected into that medium by an electrode (C) at (x_i, y_i, z_i) is given by

327

$$\begin{aligned}
328 \quad V_{ij} = \frac{I\rho_m}{4\pi} & \left\{ \frac{1}{\{X_{ij}^2 + \lambda^2[z_i - z_j]^2\}^{1/2}} + \sum_{n=1}^{\infty} \frac{k_2^{n-1}}{\{X_{ij}^2 + \lambda^2[z_i + z_j + 2(n-1)t]^2\}^{1/2}} \right. \\
329 & + \sum_{n=1}^{\infty} \frac{k_2^n}{\{X_{ij}^2 + \lambda^2[z_i - z_j - 2nt]^2\}^{1/2}} + \sum_{n=1}^{\infty} \frac{k_2^n}{\{X_{ij}^2 + \lambda^2[z_i + z_j - 2nt]^2\}^{1/2}} \\
330 & \left. + \sum_{n=1}^{\infty} \frac{k_2^n}{\{X_{ij}^2 + \lambda^2[z_i - z_j + 2nt]^2\}^{1/2}} \right\} \quad (19)
\end{aligned}$$

331

332 in which it is been assumed that $k_1 = 1$. Assuming that $\rho_m \approx 10 - 100 \, \Omega\text{m}$ and that the underlying333 sea-water has $\rho_{sw} \approx 0.4 \, \Omega\text{m}$, k_2 will be in the range of -0.92 to -0.99. The first term in (19)334 represents the potential due to the "direct path" within the anisotropic medium from C to P ,

335 whereas the four summations arise from considering the multiple "reflections" from the two

336 boundaries. Similar expressions involving both "direct path" terms and infinite series arising

337 from reflections can be deduced for the other possible combinations of locations of current and

338 potential electrodes: (i) C in the anisotropic medium, P in the underlying half-space; (ii) C in the339 underlying half-space, P in the anisotropic medium; and (iii) both C and P in the underlying half-

340 space.

3.1. Measurement of ρ_H

The effect on the measurement of ρ_H of the anisotropic medium being confined to the depth range $0 \leq z \leq t$, and there being a highly conducting half-space beneath, can be assessed by considering how potential differences calculated from expressions such as (19) compare to those that would exist in an infinite anisotropic medium. As before, the potential difference measured between electrodes in two boreholes separated by horizontal distance X_{ij} is dominated by the potential terms arising from current and potential electrodes that are in the same borehole ($X_{ij} = 0$). As above, we also consider $z_j = z_i + 0.1$. Numerical calculation shows that for the relevant likely values of k_2 the four infinite series converge after a few hundred terms. The k_2 dependence in each of the four summations means that whereas the first summation (S_1) is positive, the other three (S_2 to S_4) are negative. For a typical thickness of sea ice of $t = 1.4$ m, and $z_i = 0.1$ m (i.e. electrodes close to the upper surface of the ice) $\Sigma S_i = S_1 + S_2 + S_3 + S_4$ is positive and, approximately independently of the value of λ , about 20% of the size of the primary or "direct path" term in (19). The value of ΣS_i decreases with increasing z_i , being ~ 0 at $z_i = 0.4$ m, and negative and about 66% of the magnitude of the primary potential at $z_i = 1.2$ m, 0.2 m above the ice-water interface. Thus, even in a bounded anisotropic medium with the typical thickness and parameters relevant to sea ice it appears that estimates of the horizontal component of the resistivity are likely to be within a factor of about 2 of the true value.

To test this a synthetic dataset has been generated from the appropriate expressions such as (19) for the case of $\rho_m = 100 \text{ } \Omega\text{m}$ and $\lambda = 0.1$ (i.e. $\rho_H = 1000 \text{ } \Omega\text{m}$). The synthetic dataset comprised

over 2000 separate electrode combinations satisfying the restrictions discussed above that allow a measurement of ρ_H to be made. The synthetic data were inverted using the code Res3dinvTM produced by Geotomo Software to derive a 3D models of the horizontal resistivity structure in the volume contained between the boreholes. The code uses a smoothness constrained least-squares inversion (deGroot-Hedlin & Constable, 1990; Sasaki, 1992). Although the code allows for matrix solution using a quasi-Newton optimisation technique (Loke & Barker, 1996), all inversions were carried out using a conventional Gauss-Newton method (Loke & Dahlin, 2002) which is more appropriate in situations in which large resistivity contrasts, such as between sea ice and underlying sea water, exist. The result of the 3D inversion of the synthetic data is presented in Fig. 2 which shows both the mean value of resistivity in each 0.1 m thick layer of the derived 3D resistivity structure, and a vertical section through the structure.

It is clear from these results that, given the approximations in the theoretical development, ρ_H is indeed recovered with a good degree of accuracy at all depths within the anisotropic layer between the surface and 1.3 m depth. Only in the layer (1.3 - 1.4 m), i.e. immediately above the lower interface, is the true horizontal resistivity significantly underestimated. The low resistivity of the underlying sea water (set at 0.4 Ωm for the generation of the synthetic data) is also faithfully recovered. It should be noted that in a real situation the thickness of the anisotropic layer of sea ice is generally known from other measurements. As a result the resistivity below this depth can be constrained to the known resistivity of sea water, as has been applied in the 3D inversion the result of which shown in Fig. 2.

3.2. Measurement of ρ_m

387

388 For measurement of ρ_m , using four electrodes at the same level on the corners of a 1 m x 1 m
389 square, the situation is very different. In this case, as $X_{ij} = 1$ or $\sqrt{2}$ m, not only is the "direct path"
390 term in (19) significantly smaller, but, for typical thicknesses $t \sim 1\text{-}2$ m, all the S_i are of similar
391 magnitude and $\Sigma S_i < 0$. This results not only in the individual potentials due to current being
392 injected or removed from the medium being reduced, but also in the potential difference between
393 P_1 and P_2 being underestimated compared to the case of the infinite anisotropic medium,
394 significantly so for small values of λ . The degree of underestimation depends also on the
395 thickness, t , the depth within the ice of the electrodes being used, and, as k_2 depends upon the
396 resistivity contrast between ρ_m and the underlying sea-water, also on the actual value of ρ_m .
397 However, given the likely restricted range of values of k_2 this latter dependence is weak.

398

399 The underestimation ρ_m is illustrated in Fig. 3 which shows the results of 3D inversions of
400 synthetic data sets for different values of anisotropy λ for a thickness $t = 1.4$ m and a true value
401 of geometric mean resistivity $\rho_m = 100 \Omega\text{m}$. The electrode combinations used in generating the
402 synthetic data correspond to those applicable for the measurement of ρ_m in an infinite anisotropic
403 medium. Shown in Fig. 3, for different values of λ , are the average values of resistivity in each
404 layer of the derived 3D resistivity structure. The spatial grid used in the inversion means that in
405 each case these represent an average over 400 cells in each layer. Even for $\lambda = 0.5$, in the upper 1
406 m of the anisotropic region, the recovered value of ρ_m is only about 70% of the true value. Closer
407 to the ice-water interface the recovered value drops to about 40% of the true value. Similar, but
408 increasingly severe underestimation of ρ_m occurs for decreasing values of λ down to about 0.2.

For yet smaller values of λ the recovered value of ρ_m is of the order of only 1% of the true value and has a more complicated variation with depth.

Clearly, once a bounded anisotropic medium of typical thickness is considered, obtaining reliable measurements of geometric mean resistivity of sea ice through dc cross-borehole tomography is not necessarily straightforward. Nevertheless the generation of synthetic data sets from expressions of the form of (19) using the initial criteria for measurement of ρ_m does present a potential resolution of this problem. Inversion of such synthetic data to recover model resistivity values (hereafter referred to as ρ_m^M), makes it possible to derive an empirical parameterization of the relationship between the true value of ρ_m and the recovered value ρ_m^M for different values of t and λ . As t is generally known through independent measurement, and a good estimate of the horizontal component of the resistivity ρ_H can be recovered from cross-borehole measurements, as discussed above, this might allow both ρ_m and λ to be determined.

For example, for a given thickness t of ice the average value of resistivity at some depth, recovered from a 3D inversion of synthetic data generated for a measurement of ρ_m may be expressed as

$$\rho_m^M = F_z(\lambda)\rho_m \quad (20)$$

where $F_z(\lambda)$ is a polynomial in the anisotropy coefficient. The form of the polynomial, which describes how the derived value of resistivity, ρ_m^M , is related to the true geometric mean resistivity, ρ_m , can be determined from inversion of synthetic data sets generated for different values of λ , such as those shown in Fig. 3. Using (2) and (3) equation (20) may be expressed as

$$\rho_m^M = \lambda F_z(\lambda) \rho_H \quad (21)$$

In principal for any given situation, not only can the form of $F_z(\lambda)$ be deduced from inversion of synthetic data for the particular ice thickness, but ρ_m^M and ρ_H as functions of depth can be determined from inversion of real data. This then allows a value for λ to be found from numerical solution of (21) for each depth range in the resulting 3D models, and an estimate of the actual value of ρ_m as a function of depth can then be determined from (20).

As an example, in the depth range 0.5-0.6 m in ice of thickness 1.4 m, the results presented in Fig. 3 suggest that for $\lambda \leq 0.5$ the function $F_z(\lambda)$ can be represented to a high degree of accuracy by a fourth order polynomial

$$F_z(\lambda) = -57.411\lambda^4 + 47.077\lambda^3 - 7.1312\lambda^2 + 0.3452\lambda \quad (22)$$

For the specific case of $\lambda = 0.1$, the inversion of the synthetic data yields a value of ρ_m^M in this depth range of 0.748 Ωm . Additionally, the results in Fig. 2 show that the inversion of the separate synthetic dataset to determine ρ_H for the case $\rho_m = 100 \Omega\text{m}$, $\lambda = 0.1$ in this depth range gives a recovered value of ρ_H of 1105 Ωm . Thus (21) allows λ to be found as the numerical solution to

$$0.748 = (-57.411\lambda^5 + 47.077\lambda^4 - 7.1312\lambda^3 + 0.3452\lambda^2) 1105$$

The result is a value of $\lambda = 0.111$, impressively close to the true value of 0.1 used in the generation of the synthetic datasets.

Although the above procedure appears, at first sight, to be a resolution of the problem of determining ρ_m , there remain a number of complicating factors when applying this to a real

situation. These include (1) the structure of real sea ice may well include a variation in λ with depth which is not incorporated into the synthetic models; (2) in real sea ice the ice-water interface, modelled as a sharp boundary, is not sharply defined; (3) the reliance on the results of 3D inversions, both of real and synthetic data, may well introduce problems of resolution of resistivity structure; and (4) even in the inversions of synthetic data it is clear, for example from Fig. 3, that the derived values of ρ_m^M are relatively insensitive to λ for values of $\lambda \leq 0.1$. Quantifying the uncertainty in derived values of ρ_m resulting from these factors is non-trivial, but as a consequence it is likely that interpretation of values of ρ_m derived in the manner described above should bear in mind that these may only be correct to within a factor of the order of perhaps 3-4.

Given the degree of uncertainty introduced by the above factors it is worth considering the magnitude of resistivity changes that are likely to occur as the internal microstructure of sea ice changes due to expansion and connection of brine pockets and channels within the ice. A simple means of doing this is to consider the Hashin-Shtrikman limits (Hashin & Shtrikman, 1962) for the resistivity of a 2-phase mixture in which isolated spheres of conductivity σ_2 are surrounded by a connected matrix of conductivity σ_1 . The lower and upper limits of bulk resistivity of the mixture (occurring respectively when σ_1 or σ_2 represents the better conductor) are shown in Fig. 4 for the case of a mixture of materials with conductivities (resistivities) of 2.5 S/m (0.4 Ω m) and 0.00167 S/m (600 Ω m). As can be seen, for any volume fraction of high conductivity component above about 0.5%, the decrease in bulk resistivity between the situations of isolated high conductivity spheres (i.e. brine pores) and a connected network of high conductivity is 1-3 orders of magnitude. It is clear therefore that, in terms of tracking the changes that occur in the bulk

resistivity of sea ice as brine pores expand and connect, the ability to resolve between, for example, bulk resistivities of even 200 and 600 Ωm is not critical. In contrast the ability to distinguish bulk resistivities of 20 and 200 Ωm should enable the development of interconnected brine pore networks to be detected.

4. Field measurements on first-year landfast sea ice

To demonstrate the application of cross-borehole measurements to recovering the anisotropic resistivity structure in a real situation we present an example of measurements made on first-year landfast sea ice approximately 1 km off the coast of Barrow, Alaska at 71° 21' 56.45" N, 156° 32' 39.01" W. The measurements were made on 8-9 May 2008 as part of a sequence of six separate sets of data obtained at roughly one to two weekly intervals during April-June 2008. A sea ice mass balance site was operated by the University of Alaska Fairbanks at the same location recording snow and ice thickness, sea level, relative humidity and air, ice and water temperatures (Druckenmiller et al., 2009). The electrode strings used in the resistivity measurements were as described by Ingham et al. (2008) and were deployed at the corners of a 1 x 1 m square, allowing measurements to be made through the undisturbed sea ice between boreholes.

Measurements of the horizontal resistivity were made between each of the six borehole pairs, with each measurement involving one current and one potential electrode in each borehole according to the criteria discussed above. Thus, it is assumed that the measurements allow an accurate estimate of ρ_H , in the volume contained by the boreholes, to be derived by 3D inversion. Similarly, a combination of measurements aimed at determining ρ_m were obtained using a four

electrode array with each of the electrodes at approximately the same depth in separate boreholes, and three electrodes at the same depth in separate boreholes and a remote surface electrode. As discussed previously it is assumed that inversion of this data set yields an estimate ρ_m^M of the geometric mean resistivity which is an underestimate of the true value ρ_m .

The dataset for determination of ρ_H contained 2444 separate measurements. That for ρ_m was smaller and contained 356 measurements. The ice thickness at the time, as determined from ice temperature measurements and cores, was 1.35 m and this value was used to set the initial resistivity below this depth to approximate the resistivity of the underlying seawater (0.4 Ω m). This value was made "sticky" so as to control its degree of change during the inversions. The 3D inversion for ρ_H took 5 iterations and gave a final rms misfit of 11.8%, while that for ρ_m took 6 iterations and gave a final misfit of 1.9%. Much of the misfit in the ρ_H inversion occurs in the region of the ice-water interface. In this region the transition from high resistivity within the ice to the low resistivity sea water is clearly more complex than for the theoretical models discussed above. As a result it appears that electrodes spaced at vertical intervals of 0.1 m are not able to sample finely enough to accurately resolve the rapid change in resistivity from several hundred Ω m to a value less than 1 Ω m. The (assumed) much smaller decrease in ρ_m across this same region can, in contrast, be much better reproduced.

Sections through the resulting resistivity structures obtained from the 3D inversions showing ρ_H and ρ_m^M are presented in Fig. 5 (a) and (b) respectively. The inversions use a grid with horizontal spacing of 0.05 m in both x and y directions, and a vertical spacing of 0.1 m. Above the immediate vicinity of the ice-water interface, ρ_H is seen to be essentially uniform throughout

the body of the ice and to have a value around 600 Ωm . Some variation appears in the derived value of ρ_m^M but in general, above the ice-water interface it lies in the range 10-20 Ωm . The vertical discretisation of the model leads to sharp gradients in the recovered values of resistivity between depths of 1.3 and 1.4 m.

As discussed above, synthetic data sets generated for different values of the anisotropy coefficient allow parameterization of the degree to which, for the observed ice thickness of 1.35 m, ρ_m^M is an underestimate of the true value of the geometric mean resistivity ρ_m . Synthetic data generated for different values of anisotropy λ for the measured ice thickness of 1.35 m have been used to derive the appropriate polynomial $F_z(\lambda)$ for each depth range in the 3D models. The polynomials have then been used, with the average values of ρ_H and ρ_m^M for each layer in the resistivity models shown in Fig. 5, to estimate the actual variation of λ with depth in the ice through numerical solution of (21). These values have then been used with the values of ρ_H to determine not only the true values of ρ_m through the ice, but also to derive the vertical component of the bulk resistivity ρ_V . The standard deviations associated with the average values of ρ_H and ρ_m^M in each layer allow at least a superficial estimate of the uncertainties in λ , ρ_m and ρ_V . The results of this analysis are shown in Fig. 6 which shows the derived variation with depth of all three resistivities and the anisotropy coefficient.

The anisotropy coefficient is found to be close to 0.24 through the entire thickness of the ice down to 1.3 m depth. Although the higher values calculated between 1.3 and 1.4 m are not unreasonable given the expected increase in connectivity of brine at the base of the ice, it must

be remembered that this depth range spans the actual ice-water interface and the values of ρ_H and ρ_m^M in this region are not well resolved even though standard deviations calculated from the 3D models are relatively small. The derived values of λ are slightly less than values found, for example, by Timco (1979) at Pond Inlet, N.W.T. and Buckley et al. (1986) in the Antarctic, but are not unreasonable for sea ice formed under the quiescent conditions which tend to exist at Barrow. The corrected values for ρ_m ($\sim 150 \Omega\text{m}$) are well within the ranges previously measured by other authors using surface resistivity soundings. However, a Wenner array surface sounding taken adjacent to the location of the boreholes on 9 May 2008 yielded apparent resistivity values at small electrode spacing ($a = 0.1 - 0.4 \text{ m}$) of 40-50 Ωm , a factor of about 3 smaller than the values shown in Fig. 6. This lends some support to the suggestion that, notwithstanding the small standard deviations in the resolved resistivity values, the cumulative effect of uncertainties and approximations in the derivation of ρ_m may mean that the derived values should be regarded as an estimate correct to within a factor of 3-4. Nevertheless, in the context of mapping how the resistivity structure of sea ice varies with time over a series of measurement sequences such an unresolved ambiguity may not necessarily be crucial.

5. Summary

Sea ice is a complex medium with a microstructure that depends upon temperature, salinity and brine volume fraction (ϕ_b). The structure is also significantly affected by the conditions under which the ice forms. For example, ice formed in generally quiescent conditions shows a significant columnar structure, while more active conditions lead to a more granular structure. As a result significant differences in physical properties occur, which, given the importance of sea

ice for climate, it is crucial to understand. Additionally, the preferential alignment of brine pores within the ice means that many of these properties are anisotropic.

We have shown theoretically that suitable combinations of cross-borehole dc resistivity measurements may be used to measure directly the value of the horizontal component of the resistivity in sea ice or other anisotropic medium within which $\rho_V < \rho_H$. Furthermore, although the particular structure of sea ice means that exact measurement of the geometric mean resistivity is not possible, we have demonstrated that it is also possible to make measurements which, in association with numerical modelling, allow a reasonable estimate of ρ_m to be derived. As a consequence estimates of the vertical component of resistivity, which cannot be directly measured, can also be obtained. The technique is illustrated by an example of measurements made on first-year sea ice at Barrow, Alaska. Golden et al. (2007) have suggested that macroscopic effects of vertical fluid permeability become significant when ϕ_b is above about 5%. Previous measurements of ρ_H (Ingham et al., 2008) have suggested that a significant drop in this component of resistivity occurs when ϕ_b rises above about 8%. The development described here means that future analysis of the manner in which the resistivity structure as a whole varies with time, and contrasting and comparing this with the behaviour of other transport properties, has the potential to contribute significantly to the understanding of sea ice microstructure and its response to changes in temperature, salinity and ϕ_b .

Acknowledgements

589 KJ is supported by a Victoria University of Wellington Postgraduate Assistantship. Logistic
590 support for the field measurements was funded through NSF Arctic Sciences Grant ARC-
591 0620124 to DJP, and provided by the Barrow Arctic Science Consortium. The authors wish to
592 thank Hajo Eicken and Hugh Bibby for comments on an earlier version of the manuscript.
593

References

- Bhattacharya, P.K. and H.P. Patra (1968), *Direct current geoelectric sounding: Principles and interpretation*, 139 pp., Elsevier Publishing, Amsterdam.
- Buckley, R.G., M.P. Staines and W.H. Robinson (1986), In situ measurements of the resistivity of Antarctic sea ice, *Cold Reg. Sci. Technol.*, 12, 285-290.
- Callaghan, P.T., C.D. Eccles, T.G. Haskell, P.J. Langhorne and J.D. Seymour (1998), Earth's field NMR in Antarctica: a pulsed gradient spin echo NMR study of restricted diffusion in sea ice, *J. Magn. Reson.*, 133, 148–154.
- Callaghan, P.T., R. Dykstra, C.D. Eccles, T.G. Haskell and J.D. Seymour (1999), A nuclear magnetic resonance study of Antarctic sea ice brine diffusivity, *Cold Reg. Sci. Technol.*, 29, 153–171.
- Cherkaeva, E. and K.M. Golden (1998), Inverse bounds for microstructural parameters of composite media derived from complex permittivity measurements, *Waves in Random Media*, 8, 437-450.
- Comiso, J. C. (2003), Large scale characteristics and variability of the global sea ice cover, in *Sea Ice: An introduction to its Physics, Chemistry, Biology and Geology*, edited by D.N. Thomas and G.S. Dieckmann, pp. 112-142, Blackwell Science Ltd, Oxford.

617

618 de Groot-Hedlin, C. and S. Constable (1990), Occam's inversion to generate smooth two-

619 dimensional models from magnetotelluric data, *Geophysics*, 55, 1613-1624.

620

621 Dieckmann, G.S. and H.H. Hellmer (2003), The importance of sea ice: An overview, in *Sea Ice:*

622 *An introduction to its Physics, Chemistry, Biology and Geology*, edited by D.N. Thomas and

623 G.S. Dieckmann, pp. 1-21, Blackwell Science Ltd, Oxford.

624

625 Druckenmiller, M.L., H. Eicken, M.A. Johnson, D.J. Pringle, and C.C. Williams (2009),

626 Towards an integrated coastal sea-ice observatory: System components and a case study at

627 Barrow, Alaska, *Cold Reg. Sci. Technol.*, 56, 61-72

628

629 Eicken, H. (2003). From the microscopic, to the macroscopic, to the regional scale: Growth,

630 microstructure and properties of sea ice, in *Sea Ice: An introduction to its Physics, Chemistry,*

631 *Biology and Geology*, edited by D.N. Thomas and G.S. Dieckmann, pp. 22-81, Blackwell

632 Science Ltd, Oxford.

633

634 Eicken, H., C. Bock, R. Wittig, H. Miller and H.-O. Poertner (2000), Magnetic resonance

635 imaging of sea ice pore fluids: methods and thermal evolution of pore microstructure, *Cold Reg.*

636 *Sci. Technol.*, 31, 207–225.

637

638 Freitag, J. and H. Eicken (2003), Melt water circulation and permeability of Arctic summer sea

639 ice derived from hydrological field experiments, *J. Glaciol.*, 49, 349–358.

640

641 Fritsen, C.H., V.I. Lytle, S.F. Ackley, S.F. and C.W. Sullivan (1994), Autumn bloom of
 642 Antarctic pack-ice algae, *Science*, 266, 782-784.

643

644 Fujino, K. and Y. Suzuki (1963), An attempt to estimate the thickness of sea ice by electrical
 645 resistivity method II, *Low Temp. Sci.*, A21, 151–157.

646

647 Golden, K.M., S.F. Ackley and V.I. Lytle (1998), The percolation phase transition in sea ice.
 648 *Science*, 282, 2238-2241.

649

650 Golden, K. M., H. Eicken, A.L. Heaton, J. Miner, D.J. Pringle and J. Zhu (2007), Thermal
 651 evolution of permeability and microstructure in sea ice, *Geophys. Res. Lett.*, 34, L16501,
 652 doi:10.1029/2007GL030447

653

654 Hallikainen, M. and D.P. Winebrenner (1992), The physical basis for sea ice remote sensing, in
 655 *Microwave Remote Sensing of Sea Ice*, edited by F.D. Carsey, pp. 29-46, Geophysical
 656 Monograph, vol. 68, American Geophysical Union, Washington.

657

658 Hashin, Z. and S. Shtrikman (1962), A variational approach to the theory of the effective
 659 magnetic permeability of multiphase materials, *J. Appl. Phys.*, 33, 3125-3131.

660

661 Ingham, M., D. Pringle, and H. Eicken (2008), Cross-borehole resistivity tomography of sea ice,
 662 *Cold Reg. Sci. Technol.*, 52, 263-277.

663

664 Kawamura, T. (1988), Observations of the internal structure of sea ice by x ray computed
 665 tomography, *J. Geophys. Res.*, *93*, 2343-2350.

666

667 Keller, G. V. and F.C. Frischknecht (1966), *International series of monographs in*
 668 *electromagnetic waves Volume 10: Electrical methods in geophysical prospecting*, Pergamon
 669 Press, Oxford.

670

671 Krembs, C., R. Gradinger, and M. Spindler (2000), Implications of brine channel geometry and
 672 surface area for the interaction of sympagic organisms in Arctic Sea ice, *J. Exp. Mar. Biol. Ecol.*,
 673 *243*, 55–80.

674

675 Loke, M.H. and R.D. Barker (1996), Rapid least-squares inversion of apparent resistivity
 676 pseudosections by a quasi-Newton method, *Geophysical Prospecting*, *44*, 131-152.

677

678 Loke, M.H. and T. Dahlin (2002), A comparison of the Gauss-Newton and quasi-Newton
 679 methods in resistivity imaging inversions, *Journal of Applied Geophysics*, *49*, 149-162.

680

681 Mercier, O.R., M.W. Hunter, and P.T. Callaghan (2005), Brine diffusion in first-year sea ice
 682 measured by Earth's field PGSE-NMR, *Cold Reg. Sci. Technol.*, *42*, 96–105.

683

684 Perovich, D.K. (1998), Optical properties of sea ice, in: *Physics of Ice-Covered seas*, editor M.
 685 Lepparanta, pp. 195-230, Springer-Verlag, New York.

686

687 Pringle, D.J., H. Eicken, H.J. Trodahl, and L.G.E. Backstrom (2007), Thermal conductivity of
 688 landfast Antarctic and Arctic sea ice, *J. Geophys. Res.*, *112*, C04017,
 689 doi:10.1029/2006JC003641.

690

691 Pringle, D., G. Dubuis, and H. Eicken (2009), Impedance measurements of the complex
 692 dielectric permittivity of sea ice at 50 MHz: pore microstructure and potential for salinity
 693 monitoring, *J. Glaciol.*, *55*, 81-94.

694

695 Pringle, D. J., J.E. Miner, H. Eicken and K.M. Golden (submitted). Pore-space percolation in sea
 696 ice single crystals. *J. Geophys. Res.*

697

698 Sasaki, Y. (1992), Resolution of resistivity tomography inferred from numerical simulation,
 699 *Geophysical Prospecting*, *40*, 453-464.

700

701 Telford, W. M., L.P. Geldart, R.E. Sheriff and D.A. Keys (1977), *Applied Geophysics*,
 702 Cambridge University Press, New York.

703

704 Thyssen, F., H. Kohnen, M.V. Cowan and G.W. Timco (1974), DC Resistivity measurements on
 705 sea ice near Pond Inlet, N.W.T (Baffin Island), *Polarforschung*, *44*, 117-126.

706

707 Timco, G.W. (1979), An analysis of the in-situ resistivity of sea ice in terms of its
 708 microstructure, *J. Glaciol.*, *22*, 461–471.

709

710 Tinga, W.R., W.A.G. Voss, and D.F. Blossey, (1973), Generalized approach to multiphase
711 dielectric mixture theory, *J. Appl. Phys.*, 44, 3897-3902.

712

713 Weeks, W.F. (1998), Growth conditions and the structure and properties of sea ice in: *Physics of*
714 *Ice-Covered seas*, editor M. Lepparanta, pp. 25-104, Springer-Verlag, New York.

715

Figure captions.

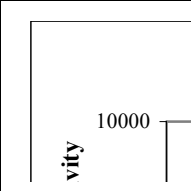
Fig. 1 Geometry for the calculation of the potential at electrode P , at (x_j, y_j, z_j) , due to current injected at electrode C , at (x_i, y_i, z_i) , for the case of a semi-infinite anisotropic medium in the region $z > 0$. The horizontal separation of the electrodes is

$$X_{ij} = \sqrt{(x_i - x_j)^2 + (y_i - y_j)^2}.$$

Fig. 2 (a) Variation of horizontal resistivity ρ_H with depth recovered by 3D inversion of synthetic borehole measurements for the case of sea ice of thickness $t = 1.4$ m, anisotropy coefficient $\lambda = 0.1$, and geometric mean resistivity $\rho_m = 100$ Ωm . The true value of ρ_H is shown by the dashed line. (b) Vertical section through the resistivity structure derived from the 3D inversion.

Fig. 3 Variation with depth of the value of geometric mean resistivity ρ_m^M recovered by 3D inversion of synthetic data sets with different values of anisotropy coefficient λ for a true value of the geometric mean resistivity of 100 Ωm and a model ice thickness of 1.4 m.

Fig. 4 Hashin-Shtrickman bounds on the resistivity of a 2-phase mixture in which one component has a resistivity of 0.4 Ωm and the other a resistivity of 600 Ωm . The upper curve shows the bulk resistivity as a function of volume fraction of the high conductivity component when that component occurs as isolated spheres, the lower



curve shows the bulk resistivity when the high conductivity component forms a connected network.

Fig. 5 Vertical sections through 3D structures of (a) ρ_H and (b) ρ_m^M derived by 3D inversion of field data collected at Barrow over May 8-9 2008. Horizontal distances and depths are both in m.

Fig. 6 Variations with depth of ρ_H , ρ_m , ρ_V and λ derived from field data collected at Barrow over May 8-9 2008. Thin lines show limits of the derived values calculated from standard deviations in the average values of ρ_H and ρ_m^M .

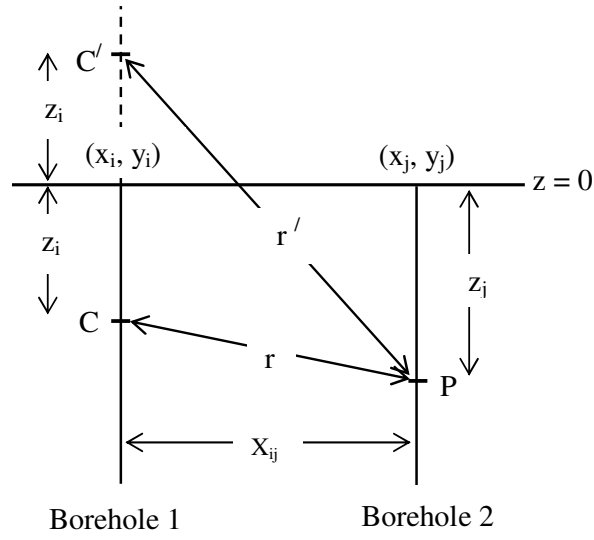


Fig. 1 Geometry for the calculation of the potential at electrode P , at (x_j, y_j, z_j) , due to current injected at electrode C , at (x_i, y_i, z_i) , for the case of a semi-infinite anisotropic medium in the region $z > 0$. The horizontal separation of the electrodes is $X_{ij} = \sqrt{(x_i - x_j)^2 + (y_i - y_j)^2}$.

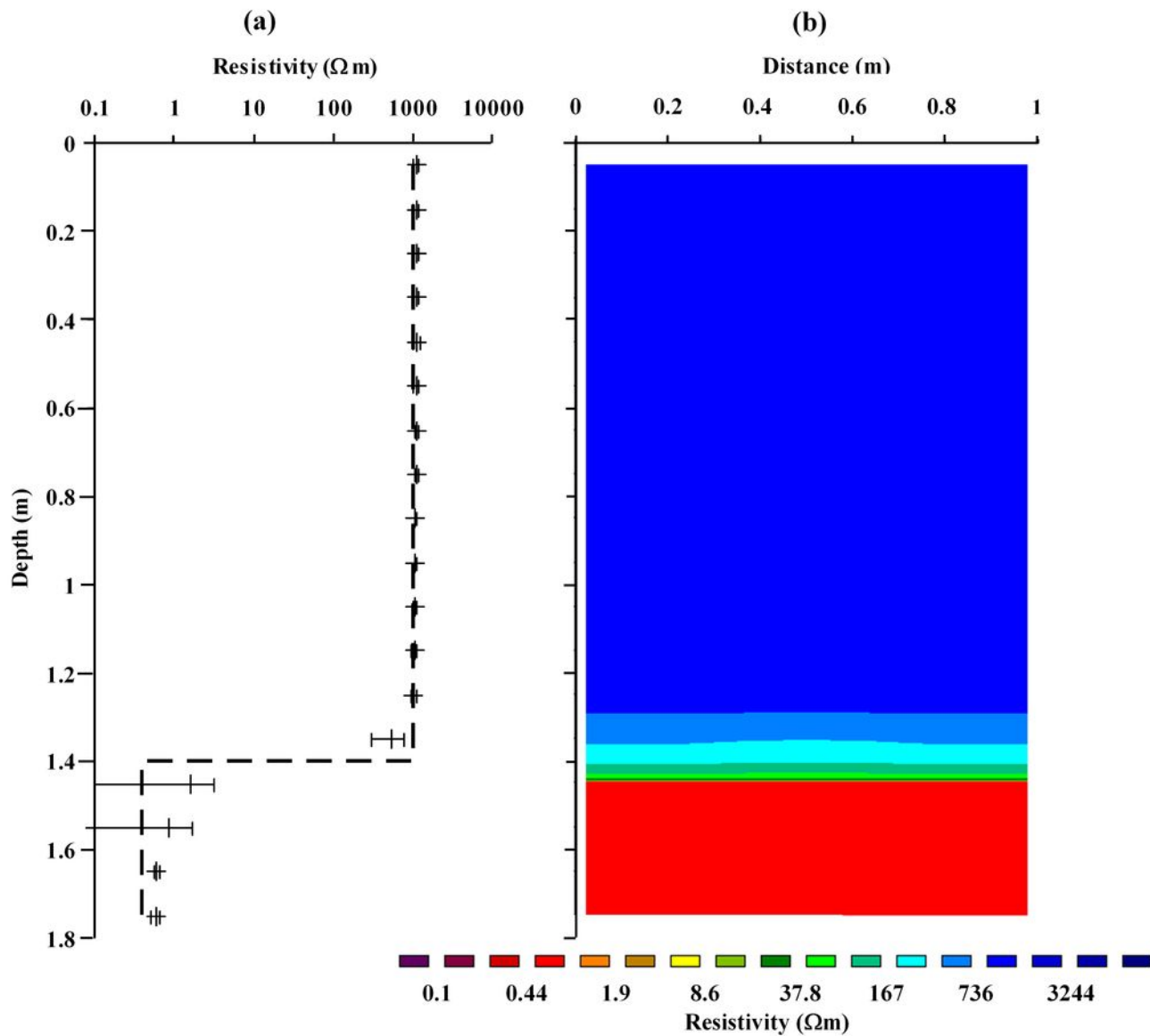


Fig. 2 (a) Variation of horizontal resistivity ρ_H with depth recovered by 3D inversion of synthetic borehole measurements for the case of sea ice of thickness $t = 1.4$ m, anisotropy coefficient $\lambda = 0.1$, and geometric mean resistivity $\rho_m = 100$ Ωm . The true value of ρ_H is shown by the dashed line. (b) Vertical section through the resistivity structure derived from the 3D inversion.

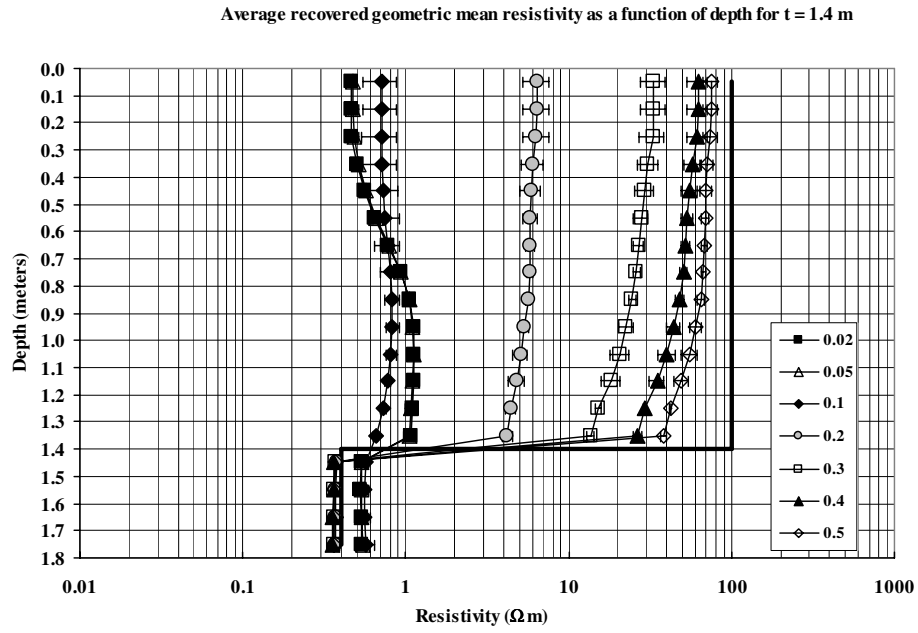


Fig. 3 Variation with depth of the value of geometric mean resistivity ρ_m^M recovered by 3D inversion of synthetic data sets with different values of anisotropy coefficient λ for a true value of the geometric mean resistivity of 100 Ωm and a model ice thickness of 1.4 m.

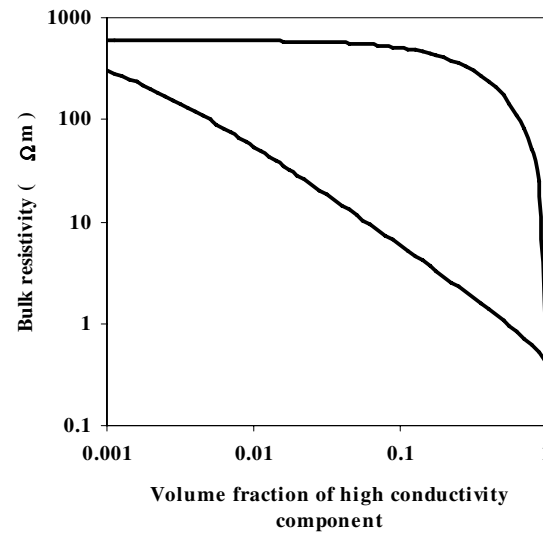


Fig. 4 Hashin-Shtrickman bounds on the resistivity of a 2-phase mixture in which one component has a resistivity of $0.4 \, \Omega\text{m}$ and the other a resistivity of $600 \, \Omega\text{m}$. The upper curve shows the bulk resistivity as a function of volume fraction of the high conductivity component when that component occurs as isolated spheres, the lower curve shows the bulk resistivity when the high conductivity component forms a connected network.

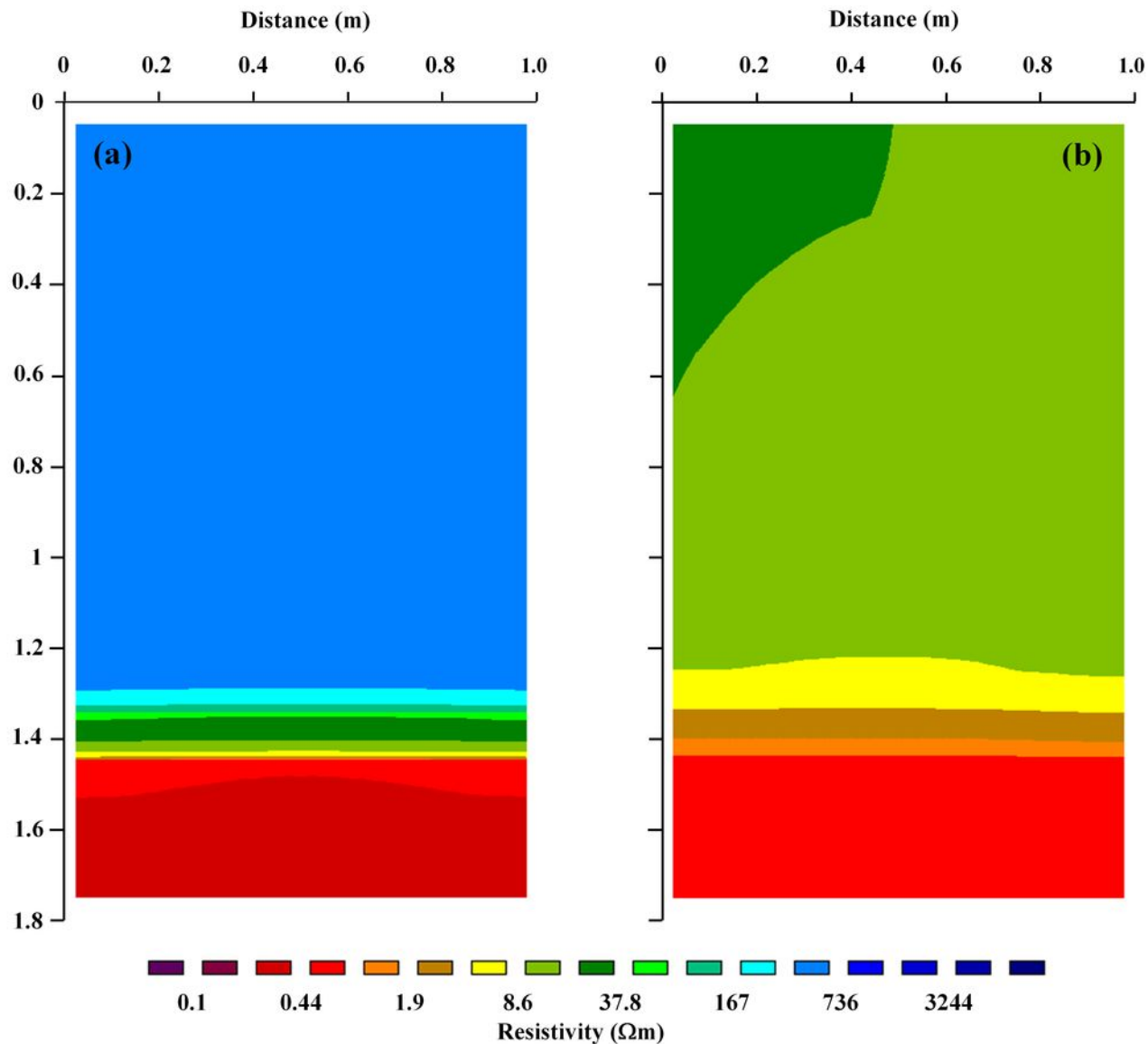


Fig. 5 Vertical sections through 3D structures of (a) ρ_H and (b) ρ_m^M derived by 3D inversion of field data collected at Barrow over May 8-9 2008. Horizontal distances and depths are both in m.

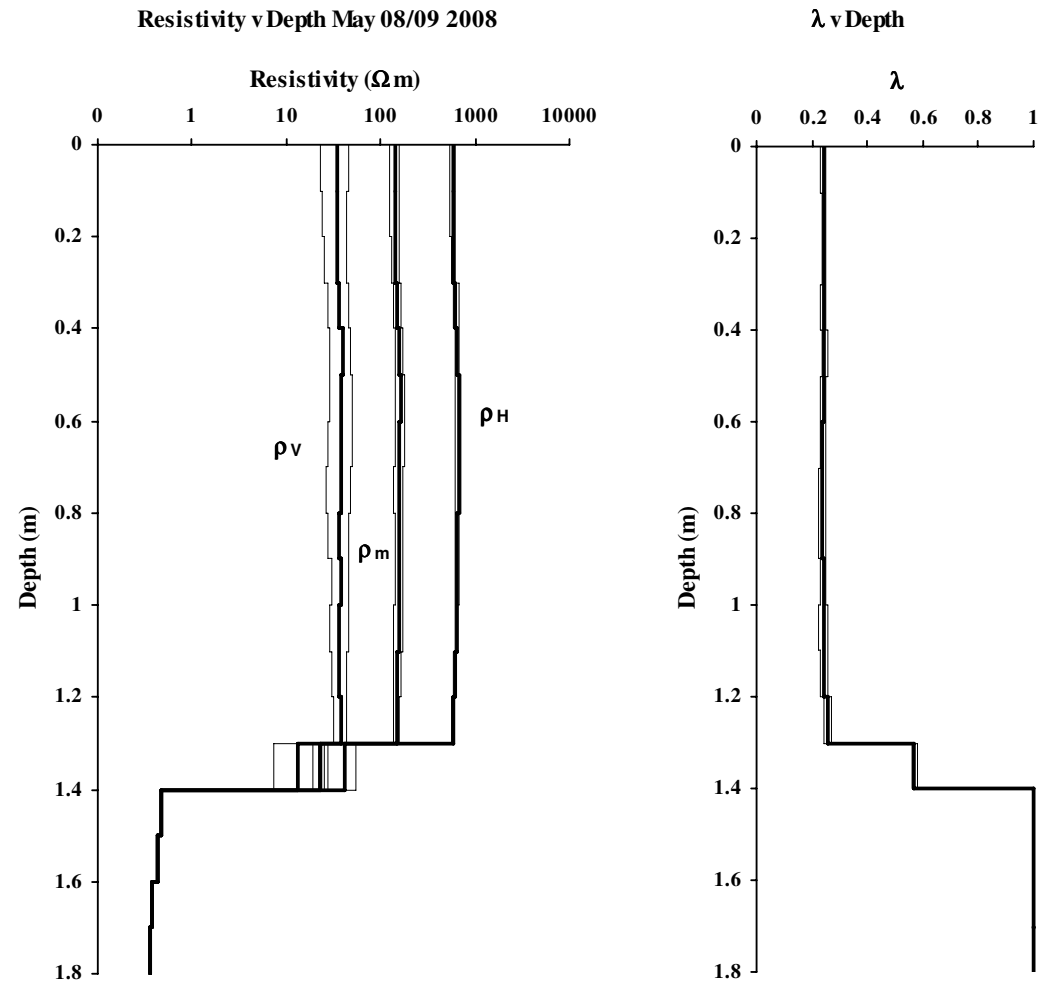


Fig. 6 Variations with depth of ρ_H , ρ_m , ρ_v and λ derived from field data collected at Barrow over May 8-9 2008. Thin lines show limits of the derived values calculated from standard deviations in the average values of ρ_H and ρ_m^M .